

# Defect Dynamics in 2-D MoS<sub>2</sub> Probed by Using Machine Learning, Atomistic Simulations, and High-Resolution Microscopy

Tarak K. Patra,<sup>†</sup> Fu Zhang,<sup>‡,§</sup> Daniel S. Schulman,<sup>‡,ID</sup> Henry Chan,<sup>†,ID</sup> Mathew J. Cherukara,<sup>†,✉,ID</sup> Mauricio Terrones,<sup>‡,§,#,⊗</sup> Saptarshi Das,<sup>\*,§,∇,ID</sup> Badri Narayanan,<sup>\*,||,II,III,ID</sup> and Subramanian K. R. S. Sankaranarayanan<sup>\*,†,✉,ID</sup>

<sup>†</sup>Center for Nanoscale Materials, <sup>||</sup>Materials Science Division, and <sup>‡</sup>X-ray Science Division, Argonne National Laboratory, Argonne, Illinois 60439, United States

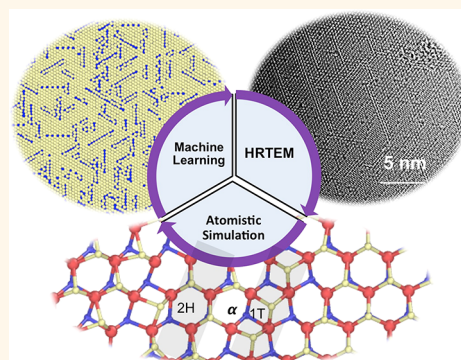
<sup>‡</sup>Materials Science and Engineering, <sup>§</sup>Center for 2-Dimensional and Layered Materials, <sup>#</sup>Department of Physics, <sup>⊗</sup>Department of Chemistry, and <sup>∇</sup>Department of Engineering Science and Mechanics, The Pennsylvania State University, University Park, Pennsylvania 16802, United States

<sup>\*</sup>Computational Institute, University of Chicago, Chicago, Illinois 60637, United States

## S Supporting Information

**ABSTRACT:** Structural defects govern various physical, chemical, and optoelectronic properties of two-dimensional transition-metal dichalcogenides (TMDs). A fundamental understanding of the spatial distribution and dynamics of defects in these low-dimensional systems is critical for advances in nanotechnology. However, such understanding has remained elusive primarily due to the inaccessibility of (a) necessary time scales *via* standard atomistic simulations and (b) required spatiotemporal resolution in experiments. Here, we take advantage of supervised machine learning, *in situ* high-resolution transmission electron microscopy (HRTEM) and molecular dynamics (MD) simulations to overcome these limitations. We combine genetic algorithms (GA) with MD to investigate the extended structure of point defects, their dynamical evolution, and their role in inducing the phase transition between the semiconducting (2H) and metallic (1T) phase in monolayer MoS<sub>2</sub>. GA-based structural optimization is used to identify the long-range structure of randomly distributed point defects (sulfur vacancies) for various defect densities. Regardless of the density, we find that organization of sulfur vacancies into extended lines is the most energetically favorable. HRTEM validates these findings and suggests a phase transformation from the 2H-to-1T phase that is localized near these extended defects when exposed to high electron beam doses. MD simulations elucidate the molecular mechanism driving the onset of the 2H to 1T transformation and indicate that finite amounts of 1T phase can be retained by increasing the defect concentration and temperature. This work significantly advances the current understanding of defect structure/evolution and structural transitions in 2D TMDs, which is crucial for designing nanoscale devices with desired functionality.

**KEYWORDS:** machine learning, microscopy, atomistic simulations, 2D materials, phase transitions, and defect dynamics



Transition-metal dichalcogenides (TMDs) exhibit versatile electronic properties and, in turn, have attracted tremendous attention for possible applications in nanoscale electronic devices.<sup>1–4</sup> In these 2D-TMDs, a myriad of structural defects can either pre-exist or be introduced during sample preparation, processing, and transfer processes. These defects can be points (*e.g.*, chalcogen vacancies) or of extended kind (*e.g.*, dislocations and boundaries); they are known to have a profound influence on the physicochemical, electronic, and optical properties of these materials.<sup>5,6</sup> For example, electrical-transport measurements on thin sheets of

MoS<sub>2</sub> almost universally reveal *n*-type field effect transistor (FET) characteristics, largely owing to the presence of chalcogen vacancies, impurities, and metal-like antisite defects that pin the Fermi level of the metal at the metal/TMD contact interfaces.<sup>7–10</sup> In addition, a high defect density is strongly correlated with low carrier mobility<sup>11–13</sup> as well as

Received: April 16, 2018

Accepted: August 3, 2018

Published: August 3, 2018

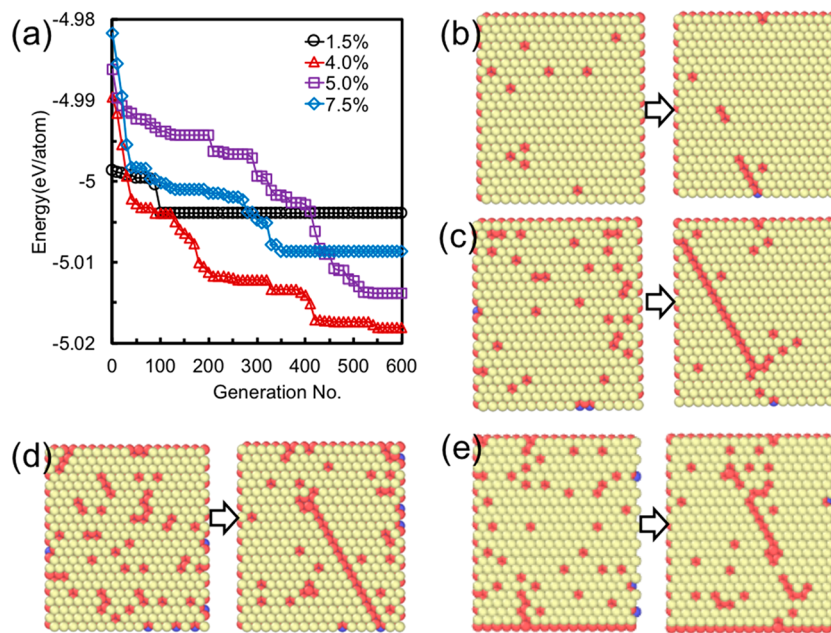


**Figure 1.** Evolutionary search for optimal extended defect configurations at various concentrations of S vacancies, achieved using genetic algorithms. (a) Potential energy of the most stable configuration is plotted as a function of generation at various defect concentrations. The defect concentration is evaluated as the fraction of the available S sites that are vacant. The initial and final configurations of four evolutions are shown in (b), (c), (d), and (e) for concentrations of 1.5%, 4.0%, 5.0%, and 7.5%, respectively.

hysteresis in FET characteristics, since they act as adsorption sites for chemical species. While defects are considered detrimental for conventional high-performance electronic devices, precise control over the density and distribution of defects may open up avenues for electronic applications, such as neuromorphic devices.<sup>14,15</sup>

Previous experimental and theoretical studies suggest that the most abundant defect in TMDs, such as MoS<sub>2</sub>, is the chalcogen (sulfur) monovacancies. These point defects often reorganize to form extended structures during sample processing, transfer, as well as operation of a device; atomic-scale dynamics of these extended defect structures control key structural transitions.<sup>16</sup> Of particular interest is the defect-mediated crossover between 2H (semiconductor) and 1T (metallic) phases of MoS<sub>2</sub> mainly owing to its immediate relevance to nanoscale device applications.<sup>17–19</sup> The reorganization of point defects necessary for 2H-to-1T transition can be triggered *via* operating/processing conditions of heating, prolonged-electron beam irradiation, or lithiation.<sup>17–19</sup> Structurally, 2H phase possesses a trigonal prismatic arrangement of a molybdenum (Mo) atom sandwiched between two sulfur (S) atoms, while the 1T phase exhibits an octahedral coordination.<sup>20</sup> In addition to different electronic properties, the two phases also exhibit contrasting magnetic behavior; 1T phase is paramagnet, while 2H phase is weakly diamagnetic.<sup>21</sup> A precise control over this phase transition is of great interest to make specific spatial patterns of 1T/2H domains, such as placing low resistance 1T phase electrical contacts with an atomically sharp interface to the semiconducting 2H channel in FETs.<sup>22</sup> The 2H and 1T phase can coexist in a single-layer MoS<sub>2</sub>, and the relative fractions can be varied to tune their optoelectronic and electrocatalytic properties. For example, when the contents of the 1T phase increase, the photoelectric conversion efficiency of a MoS<sub>2</sub>-based photo anode increases,<sup>23</sup> the performance of a MoS<sub>2</sub> based supercapacitor improves,<sup>24</sup> and the efficiency of WS<sub>2</sub> nanosheets for hydrogen evolution reactions (HER) is

enhanced.<sup>25</sup> Interestingly, the defect distribution in a Li-intercalated MoS<sub>2</sub> sheet can also be altered by sonication<sup>26</sup> and solvent thermal treatment to reverse the transformation from the 1T to the 2H phase.<sup>27</sup> Evidently, a fundamental understanding of the atomic-scale structure and dynamics of defects in 2D TMDs as well as their role in phase transitions is very crucial for device applications. However, such an understanding has remained elusive until now.

The transition between 2H and 1T phases involves local rearrangement of S atoms with respect to their central Mo atom. A previous study on Re-doped MoS<sub>2</sub> reports that the 2H-to-1T transition proceeds *via* formation (and subsequent intersection) of an intermediate alpha ( $\alpha$ ) phase under electron-beam radiation at high temperatures.<sup>16</sup> Although this work characterized the structure of  $\alpha$ -phase to contain a shrunk zig-zag pattern of Mo atoms,<sup>16</sup> the key question as to why such an intermediate phase is required for the 2H to 1T phase transformation remains unanswered. Recent density functional theory works have shown that the 2H-to-1T phase transition is associated with a finite energy barrier, with 2H being the energetically most favorable phase;<sup>28</sup> they postulate that the electron transfer between MoS<sub>2</sub> and the dopants initiate the 2H-to-1T transformation.<sup>29</sup> However, the molecular mechanisms underlying the 2H-to-1T transition, the role of defects, as well as the dynamical evolution/rearrangement of S and Mo atoms during this phase transformation have not yet been established. The major challenge in addressing these questions is that the atomic-scale processes governing formation of extended defects, and phase transition involves a broad range of time scales from picoseconds to several seconds or minutes. The shorter time scales (picoseconds) can be accessed *via* ultrafast synchrotron X-ray experiments, such as coherent diffraction imaging. Although our recent study using coherent diffraction imaging at state-of-the-art synchrotron facilities has been successful in investigating multilayered 2-D dichalcogenides,<sup>30</sup> the spatial resolution is limited to 10

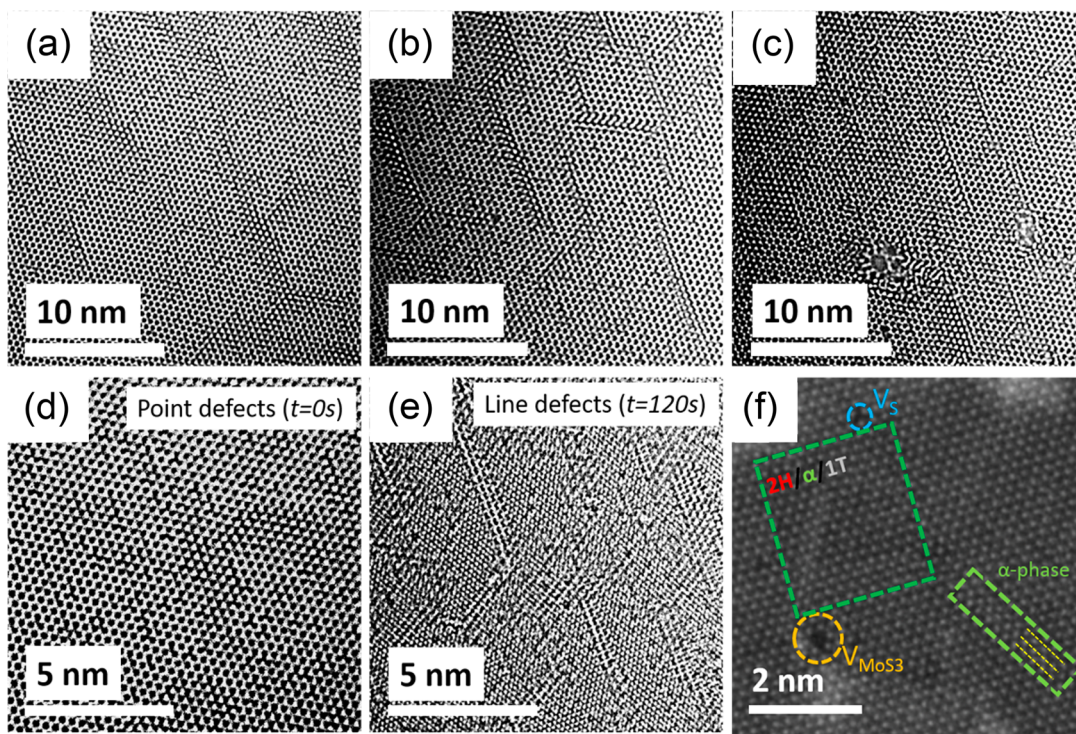


**Figure 2.** High-resolution TEM images showing the distribution of line defects in MoS<sub>2</sub> samples with different defect densities: (a) light, (b) medium and (c) heavy. Extended line defects identified by our GA search are seen in this HRTEM images of MoS<sub>2</sub>. Defect distribution under electron beam ( $\sim 50000 \text{ e}^-/\text{\AA}^2\cdot\text{s}$ ) are shown in (d) and (e) at time  $t = 0 \text{ s}$  and  $t = 120 \text{ s}$ , respectively. (f) Atomic-resolved HAADF-STEM image of monolayer MoS<sub>2</sub> shows various defect configurations.

nm, which makes it difficult to track point defects. High-resolution transmission electron microscopy (HRTEM), on the other hand, possesses the necessary resolution to image point defects; but cannot capture ultrafast dynamics owing to its slow frame speed ( $\sim 10 \text{ Hz}$ ). Standard atomistic simulations (e.g., molecular dynamics) have atomic resolution but are limited to several tens of nanoseconds.

Here, we use machine learning, molecular simulations, and high-resolution transmission electron microscopy (HRTEM) to overcome these limitations. We investigate the energetics of arrangement of point defects into extended line defects at various S-vacancy concentrations and subsequently elucidate the role of these extended defects in the 2H-to-1T phase transformation. A genetic algorithm (GA) is used to efficiently search the most energetically favorable distribution of atomic defects, wherein the energies of individual candidate structures (genes) are calculated using a reactive force field. The stable structures identified by our evolutionary search are experimentally verified via HRTEM. We then investigate the gliding and rearrangement of S and Mo atoms around the regions of extended defects in the MoS<sub>2</sub> layer via molecular dynamics (MD) simulations. These MD simulations identify the molecular mechanisms governing  $\alpha$ -phase formation near the extended defects in 2H-MoS<sub>2</sub> and its influence on the subsequent transition to the 1T phase. Furthermore, our large-scale MD simulations demonstrate the impact of temperature on the size, shape, and concentration of 1T phase domains in the monolayer. In addition, we observe that such a transformation is absent in randomly distributed S-vacancies in a MoS<sub>2</sub> layer. Overall, our study elucidates atomic-scale dynamics associated with defect migration, provides a mechanism for 2H-to-1T transformation, and outlines useful

design rules for engineering the properties of 2D materials by deviating from their stoichiometric composition.

## RESULTS AND DISCUSSION

**Evolutionary Structural Optimization of Defects in 2D MoS<sub>2</sub>.** We first track the extended configurations of sulfur vacancies in a monolayer MoS<sub>2</sub> by performing GA-based structural optimization. Our search for extended configurations made up entirely of S vacancies is well-founded in light of recent experiments, which indicate that S vacancies are the most dominant type of defects in MoS<sub>2</sub> sheets obtained *via* mechanical exfoliation and chemical vapor deposition.<sup>31</sup> Furthermore, previous DFT calculations report that the formation energies of S-vacancy (2.12 eV) are lower than all other types of defects including anti-sites.<sup>5</sup> As mentioned here, we start our GA runs with initial populations of candidates containing randomly distributed S-vacancies at the desired vacancy density. Figure 1 shows the evolution of defect structures from randomly dispersed vacancies to ordered extended configurations in a MoS<sub>2</sub> monolayer at four different S-vacancy concentrations ( $\rho = 1.5, 4, 5$  and 7.5%). The potential energy of the most stable structure obtained at each generation is plotted in Figure 1a, which converges in  $\sim 600$  generations for all of the cases. Parts b–e of Figure 1 depict the atomic snapshots of initial randomly distributed S-vacancies and final optimized configurations at various vacancy concentrations. During the early stages of evolution (within first  $\sim 100$  generations), we observe formation of small aggregates of vacancies, such as dimers and trimers. The energetic gain in forming these aggregates is  $\sim 0.001 \text{ eV}/\text{atom}$  for  $\rho = 1.5\%$  and  $0.018 \text{ eV}/\text{atom}$  for the highest concentration studied, *i.e.*,  $\rho = 7.5\%$ . The number of dimers and trimers is a

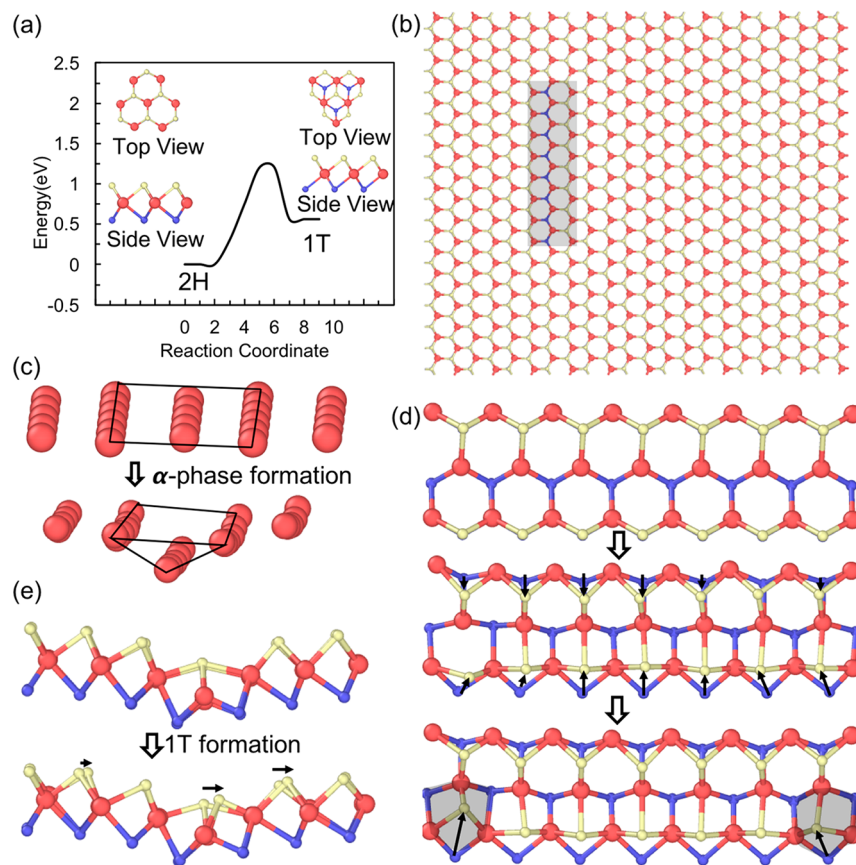


**Figure 3.** Role played by line defects in 2H-to-1T phase transition in MoS<sub>2</sub>. (a) Energy barrier associated with the 2H-1T transition.<sup>29</sup> (Inset) Top and side view of the two phases are shown schematically. (b) Initial configuration of a line defect in a 2H-MoS<sub>2</sub> layer of dimension 5.8 nm × 5.2 nm. The line defect is shaded for clarity. (c) Evolution of Mo atoms proximal to line defect at 900 K. (d) S atoms in one plane glide with respect to other leading to rapid shrinking of Mo–Mo bonds near the line defect forming an intermediate  $\alpha$ -phase. (e) Side view of S atoms gliding over longer time scales results in 1T phase. Mo atoms are shown in red whereas atoms in yellow represent top layer of S and atoms in blue represent bottom layer of S.

strong function of the defect density and shows a non-monotonic trend; the highest fraction of vacancies occurs in the form of dimers/trimers (~3%) for  $\rho = 7.5\%$  after  $\sim 130$  generations. As the GA run proceeds further, we observe that most of the vacancies exist as small line defects (~3–4 S vacancies). Depending on the defect densities, we also observe a rich variety of configurations, including triangular shapes (Figure 1d) or zig-zag (Figure 1e). This is consistent with previous experiments, which report the existence of triangular holes,<sup>32,33</sup> flower shapes,<sup>34</sup> and amorphous networks,<sup>35</sup> along with lines in electron-beam irradiated 2D materials. Additionally, triangular holes formed by three missing neighboring sulfur atoms (Figure 1d) suggest the possibility of a V<sub>MoS<sub>3</sub></sub> phase in a MoS<sub>2</sub> layer as seen in our HRTEM; both of these findings are consistent with previous experimental works.<sup>5</sup> The lowest energy structures obtained at the end of the GA runs reveal extended line defects of sulfur vacancies (>10) to be the most favorable at all vacancy concentrations considered in this work (Figure 1b–e). The energies of the optimized defect structures are 5.0034, 5.01844, 5.0195, and 5.00866 eV/atom lower than the initial random population for  $\rho = 1.5\%$ , 4.0%, 5.0%, and 7.5%, respectively.

The energy of the most stable structure is expected to increase monotonically with defect concentration. Indeed, the lowest energy of GA-optimized configurations, for  $\rho \geq 4\%$ , follow this intuitive trend. At the lowest defect concentration

studied here (*i.e.*,  $\rho = 1.5\%$ ), however, the converged energy value is higher than all of the other cases, which is counterintuitive. The GA-identified lowest energy configuration (after 600 generations) for  $\rho = 1.5\%$  consists of a combination of lines (of varying sizes) and isolated vacancies (*cf.* Figure 1b), which results in a somewhat higher energy  $\sim -5.0034$  eV/atom. Ordering all of the vacancies in a single line, for  $\rho = 1.5\%$ , results in a drop of  $\sim 17$  meV/atom, yielding an energy value of  $-5.021$  eV/atom, lower than that of higher defect concentrations ( $\rho \geq 4\%$ ). Thus, the GA run for  $\rho = 1.5\%$  does not reach the global energy minimum within 600 generations. Nevertheless, it is important to note that the energetic difference between the configuration shown in Figure 1b and the global minimum ( $\sim 17$  meV/atom) is within the thermal fluctuations at room temperature. Thus, extended defect configurations containing lines of different lengths (such as that identified by GA in Figure 1b) are all likely to occur at room temperature, alongside the global minimum structure. This finding is firmly supported by our HRTEM images (Figure 2), which show a range of defect configurations with lines of varying lengths, along with isolated defects. We further note that the slow convergence of GA for low defect concentration case (*i.e.*, extremal cases) is typical of most ML methods.<sup>36</sup>

**High-Resolution Electron Microscopy on Defect Evolution and Distribution in MoS<sub>2</sub> Samples.** We

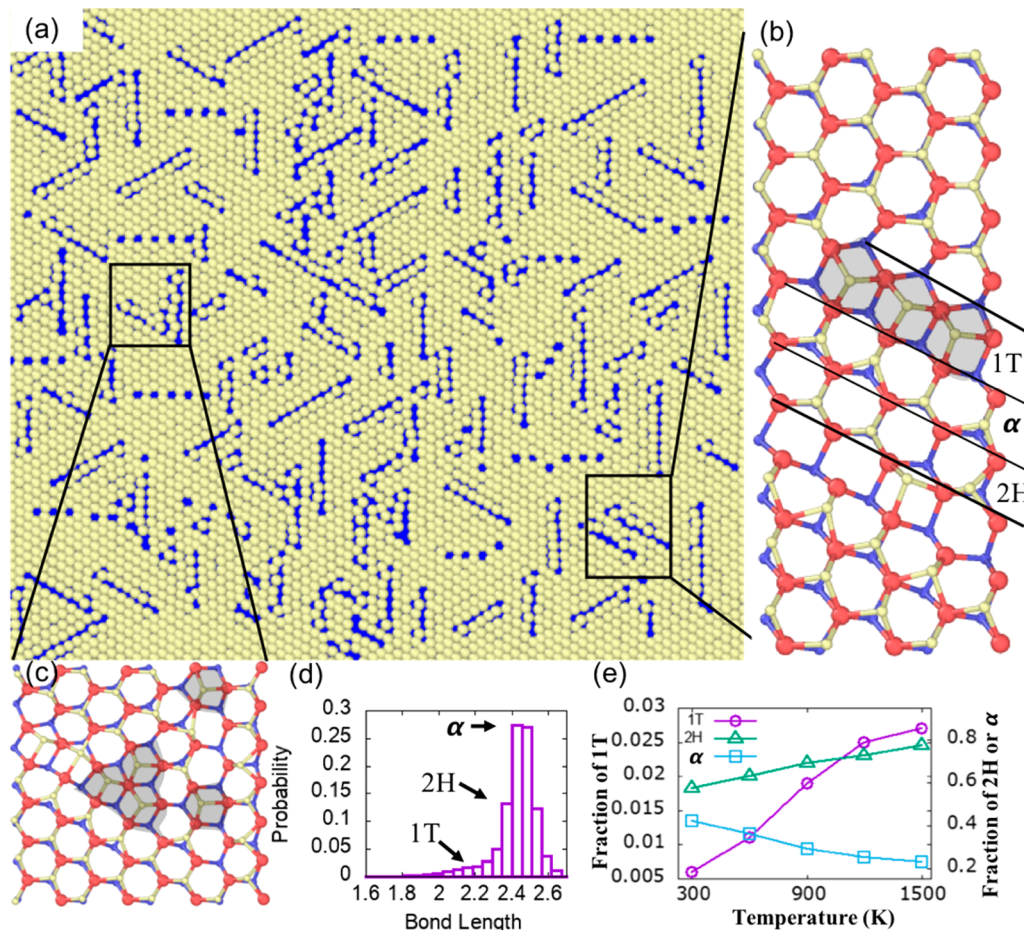


**Figure 4.** Phase transformation on a MoS<sub>2</sub> layer with randomly distributed line defects. (a) Atomic snapshot after 1 ns of MD simulation at 900 K. The top view of the sheet is shown where blue regions represent extended defects, and yellow beads are the S atoms in the top layer. Two zoomed regions in (a) are highlighted in (b) and (c) with atomic details. The coexistence of 2H, 1T, and  $\alpha$  phases are demonstrated in (b) where solid lines are guide to the eye. Further, 1T phases are shaded for clarity in (b) and (c). (d) Probability distribution of bonds between Mo atoms and top layer S atoms at 900 K, where the bond lengths corresponding to 1T, 2H, and  $\alpha$  are shown by arrow marks. (e) Fraction of 1T, 2H, and  $\alpha$  phases as a function of temperature.

performed detailed characterization of the defect distribution in 2D MoS<sub>2</sub> to validate the structural predictions made by our GA. Three electroablated monolayer MoS<sub>2</sub> regions with different defect densities were imaged by HRTEM with a large overfocus imposed to ensure the bright atom contrast and easily distinguish the defects from perfect hexagonal lattice. The structural defects evolve from randomly distributed sulfur monovacancies (light defect density shown in Figure 2a) and distributed line defects (medium density shown in Figure 2b) to extended coupled line defect induced structural disorders (heavily defective structure shown in Figure 2c). Such HRTEM observations testify the GA prediction at different defect densities in 2D MoS<sub>2</sub> and indicate a large variation in the size of extended defects. We note that these defects are intrinsic in the sample as the doses used for beam shower and imaging are mild ( $\sim$ 5000 e<sup>-</sup>/Å<sup>2</sup>·s) and unlikely to create knock-on damages. However, prolonged electron irradiation in the monochromated TEM mode ( $\sim$ 50000 e<sup>-</sup>/Å<sup>2</sup>·s for 120 s, which is 1-fold higher than the imaging dose, demonstrated in Figure 2a–c) generates sulfur monovacancies due to the knock-on damage.<sup>37</sup> This prolonged electron irradiation helps randomly distributed sulfur monovacancies to evolve into extended structural imperfections such as line defects, triangular holes, and amorphous networks as shown in Figure

2d,e. Further, an atomic-resolution high-angle annular dark field scanning TEM (HAADF-STEM) image of the irradiated monolayer MoS<sub>2</sub> in Figure 2f shows various defect configurations such as sulfur monovacancies V<sub>S</sub> and triangular defects V<sub>MoS<sub>2</sub></sub>. Figure 2f also suggests the formation of an  $\alpha$ -phase due to extensive line defects, and coupling of two  $\alpha$ -phase regions at 60° to each other may trigger the formation of 1T domains in the 2H phase of MoS<sub>2</sub>.<sup>16</sup>

**Atomistic Simulations of Defect-Driven 2H-to-1T Phase Transformation.** Our HRTEM characterization reveals a rich distribution of extended defects and hints at a possible correlation between the defect densities and the observed phases (2H, 1T and  $\alpha$ ). This correlation is also observed for many other 2D materials.<sup>31</sup> Here, we aim to understand this correlation for MoS<sub>2</sub> monolayers. The 2H phase of MoS<sub>2</sub> exhibits ABA staking of atoms, while the atoms are in an ABC staking in the 1T phase as shown in Figure 3a.<sup>20</sup> Both DFT and ReaxFF calculations suggest an energy difference of 0.5 eV per formula unit that exists between the two phases, with 1T and 2H being the metastable and ground states, respectively. Further, Nudged Elastic Band calculations shown in Figure 3a indicate that an energy barrier of 1.25 eV per formula unit needs to be surmounted in order to transform from a 2H phase to a 1T phase.<sup>20</sup> On the other hand, the

energy barrier for the  $1T \rightarrow 2H$  phase transformation is 0.75 eV per formula unit. Such barriers can be surmounted *via* heat treatment, which in turn can yield coexistence of 2H and 1T phases in the same sample.<sup>19,38,39</sup> This is especially important considering the widely different electronic properties of the 2H and 1T phases. Previous studies suggest that the transformation between the 2H and 1T phase requires gliding of S atoms in one plane with respect to the other; such gliding can be achieved by thermal activation, and exposure to an electric beam.<sup>40</sup> Here, we explore the effects of extended line defects seen in our GA and HRTEM on the phase transformation between the 2H and 1T phases. In particular, we perform MD simulations to better understand how the gliding of atoms takes place during the transformation and gain insights into the atomic scale pathways *via* which the energy barrier is surmounted in a MoS<sub>2</sub> layer during heat treatment. We first perform a series of controlled MD simulations on pristine phases. Our MD simulations on the pristine 1T phase and 2H phase do not show any transformation, regardless of the temperature (*cf.* Figure S1, Supporting Information). Furthermore, randomly distributed atomic defects on these two phases do not induce a phase transformation (*cf.* Figure S2, Supporting Information). Next, we perform MD simulations on configurations with extended line defects. These simulations demonstrate that phase transformation initiates only when extended defects appear on a MoS<sub>2</sub> layer, which is identified as the lowest energy configuration by our GA study. We performed a series of MD simulations at different temperatures starting with configurations that have randomly distributed line defect(s) (similar to GA predictions) in a MoS<sub>2</sub> layer. Parts b–e of Figure 3 illustrate the atomic-scale mechanisms for the onset of the 2H-to-1T transition in a MoS<sub>2</sub> sheet with a single line defect, as identified by our MD simulations. The initial configuration is entirely 2H containing a line defect (Figure 3b), with a configuration similar to that obtained from our evolutionary structural searches (Figure 1b–e). The temporal evolution of the region proximal to the line defect is shown in Figure 3c. We observe two types of phase transformations that have widely different time scales. There is an initial rapid formation of the so-called  $\alpha$  phase near the line defect within the first 10 ps of the MD run. During this  $\alpha$ -phase formation, top S atoms from both sides of the line defect glide toward the defect, as shown by the solid black arrows in Figure 3. The gliding of S atoms is concurrent with the shrinking of Mo atomic lines in the middle layer of the sheet (Figure 3d). Over much longer time scales (~1 ns), the 1T phase starts to nucleate near the  $\alpha$  region, which is highlighted by shaded regions in the bottom panel of Figure 3c. In addition, the gliding of S atoms during the 1T phase formation (side view) is shown by solid arrows in Figure 3e. Such coexistence of the 2H, 1T, and  $\alpha$ -phase is also seen in our HRTEM experiment (*cf.* Figure 2).

In order to understand the kinetics associated with local growth of the 1T phase and its stability, we perform large-scale MD simulations where line defects are randomly placed in a 21.8 nm × 24.9 nm MoS<sub>2</sub> sheet. This large sheet of MoS<sub>2</sub> represents a distribution of extended line defects (identified by GA) that are in close agreement with HRTEM images shown in Figure 2. The equilibrium configuration of the large area MoS<sub>2</sub> sheet is shown in Figure 4a for a representative temperature (900 K). The system reaches a steady state within ~1 ns, wherein 1T, 2H, and  $\alpha$  phases coexist (Figure 4a,b). Similar to the single-line defect system, we also observe

transformation of the 2H phase to 1T phase locally near the line defects. In particular, discrete linear regions (one-dimensional) of the 1T phase form next to the  $\alpha$ -phase; a representative region close to a line defect that transforms to 2H- $\alpha$ -1T is shown in Figure 4b. Furthermore, two-dimensional growth of 1T phase is seen at the intersection of two-line defects, as shown in Figure 4c. This observation is consistent with the findings of our HRTEM images (Figure 2f). Next, we analyze the distribution and amounts of various phases as a function of temperature. We use a distance criterion to distinguish different phases after the MoS<sub>2</sub> layer reaches a steady state at any given temperature. The Mo and S atoms belonging to 1T, 2H, and  $\alpha$ -phases are distinguished using the shortest Mo–S separation distances (1T: 2.18 Å, 2H: 2.33 Å and  $\alpha$ : 2.45 Å). The detailed in-equilibrium configurations and interatomic distances for various phases in a MoS<sub>2</sub> monolayer can be found elsewhere.<sup>20,41,42</sup> The probability distribution of different phases at 900 K is shown in Figure 4d. At 900 K, 14% of Mo–S bonds correspond to the 2H phase, while 1.7% of the Mo–S bonds correspond to the 1T phase. A large portion of Mo–S bonds (26%) remains in the  $\alpha$ -phase, which may transform into the 1T phase over extended time scales not accessible to MD simulations. Our simulations further suggest that the relative proportions of the three phases can be controlled by varying the temperature. For example, the proportion of the 1T and 2H phase increases with temperature as shown in Figure 4e. The data suggest that the rate of increment in 1T phase is greater than that of 2H phase. The increment in the proportion of the 2H and 1T phase is due to the reduction of  $\alpha$ -phase as temperature increases.

Figure 4e shows that the fraction of 1T phase is low (0.5%–2.5%) regardless of the temperature; nevertheless, even this small amount of metal region has a significant impact in device application. It has the potential to significantly decrease the Schottky barrier and strong Fermi level pinning on the extended defects.<sup>9</sup> Therefore, creating such a small domain of a local conducting region is very important for many device applications such as making a conducting filament in a large TMD layer for neuromorphic devices. Furthermore, we expect that the fraction of 1T phase can be tailored by changing the distribution of extended defects, and alignment of extended defects within a particular distribution. Our findings clearly demonstrate the possibility of controlling the size and shape of 1T phases by manipulating the defect densities, temperature, and/or alignment of extended defects.

## CONCLUSIONS

Evolution of point defects into extended defects and their role in inducing phase transformation in an atomically thin sheet of a TMD layer involves atomic processes that occur over a broad range of time scales spanning picoseconds to several seconds. Traditional experimental and simulation methods often fail to provide a holistic understanding of such multiscale phenomena. Here, we combine machine learning, molecular dynamics simulations, and high-resolution electron microscopy to fully understand phase transformation in a TMD layer. In particular, we investigated the defect distribution and their role in driving the 2H-to-1T phase transformation using MoS<sub>2</sub> as a model TMD material. The genetic algorithm identifies the aggregation of point defects (0D) into a line defect (1D) on a MoS<sub>2</sub> layer, which is the energetically most stable structure; such aggregation of point defects into ordered line defects occurs regardless of the vacancy concentration. These predictions are

validated by our *in situ* HRTEM experiments. The HRTEM experiments suggest a possible semiconductor (2H) to metal (1T) phase transformation locally in the vicinity of the line defect. We conduct MD simulations that elucidate the molecular mechanism of this defect-driven phase transformation. Our simulations reveal that the S atoms glide locally toward the defect sites and lead to the formation of an intermediate  $\alpha$ -phase. This  $\alpha$ -phase triggers 1T phase formation locally. We demonstrate that a typical 2H  $\rightarrow$  1T phase transformation in a MoS<sub>2</sub> layer is associated with phenomena occurring over several different time scales: (i) a long time, typically seconds and minutes, over which atomic defects migrate and coalescence into extended line defects, (ii) a rapid transformation of 2H to  $\alpha$ -phase ( $\sim$ 10 ps) around these extended line defects, and (iii) an intermediate time scale (1 ns), over which the  $\alpha$ -phase initiates the 2H  $\rightarrow$  1T phase transformation. The coalescence of point defects and formation of 1T require activation energy, which is typically provided through heating and electron beam radiation in experiments. Therefore, by introducing line defects, the relative proportions and the coexistence of metallic 1T and semiconducting 2H phases can be systematically tuned in an atomically thin MoS<sub>2</sub> layer. Our HRTEM and MD simulations suggest that the size and shape of the 1T regions is influenced by the alignment of the extended line defects. Overall, the present study elucidates the defect aggregation and defect driven phase transition mechanism in 2D TMD materials. This has potential implications in fabricating electrical circuits in the semiconducting MoS<sub>2</sub> monolayer for nanoscale electronic applications. In addition, our work provides a generic framework where machine learning can be combined with molecular simulations and electron microscopy to study multiscale processes associated with complex materials phenomena.

## METHODS

Over the past few years, machine learning and artificial intelligence based methods have advanced various facets of materials science, including accelerated synthesis *via* robotics,<sup>43</sup> enhancing existing material characterization methods,<sup>44</sup> searching for thermodynamically stable structures,<sup>45,46</sup> materials design,<sup>36,47</sup> and developing accurate atomistic models.<sup>48–50</sup> In the context of 2D materials, such ML-based techniques have enabled rapid searches for exfoliated 2D monolayers and their assembly into superlattices/heterostructures<sup>43</sup> as well as enhancing optical characterization of large-area 2D materials.<sup>44</sup>

Simulation methods such as ab initio molecular dynamics (AIMD) simulations, classical MD, and kinetic Monte Carlo simulations can be used to understand defect dynamics. AIMD simulations due to their high cost are limited in the time and length scales they can access. Some of our recent studies push the limit of what can be achieved with AIMD<sup>51–53</sup> (we note that these simulations were performed on Argonne's leadership computing and a single simulation required 10000 cores over 6 months for simulation time scales of few tens of picoseconds). Clearly, studies of defect dynamics (approximately several nanoseconds and longer) remain intractable with AIMD. Kinetic Monte Carlo is a powerful mesoscale technique to access much larger length scales and longer time scales but relies on knowledge of a predefined rate catalog; *i.e.*, mechanisms have to be known *a priori*.<sup>54,55</sup> Classical MD overcomes these limitations and allows us to understand extended defect dynamics over nanometer/nanosecond scales. While there are reports of machine learning enhanced molecular dynamics (MD) simulations (*i.e.*, the use of machine learning to develop accurate interatomic potentials for use in MD simulations), this work uses machine learning to perform structural optimization and evolution of the point defects into extended structures. Essentially, this work involves use of GA to

sample configurations of defect structures to identify ones that are energetically favorable; in the case of our target system MoS<sub>2</sub>, the line defects (ordered vacancies) are more stable than isolated vacancies (*i.e.*, point defects). For instance, GA has been used to obtain optimal potential parameter sets for a bond-order potential to describe interactions in Co–C heterostructures.<sup>50</sup> Similarly, Csányi *et al.*<sup>56</sup> employ machine learning to construct force-field models for amorphous silicon, while Ramprasad *et al.*<sup>48</sup> provide a perspective on the use of machine learning to develop interatomic potentials for various materials. In short, these works (and other related report) involve designing strategies for efficient parameter optimization, while we are focused on deriving the most stable structural configuration of extended defects.

It should be noted that structural optimization *via* GA has also been used for 2D science mainly for crystal-structure prediction.<sup>36,47,57–59</sup> In most studies, genetic algorithm (GA) in combination with density functional theory (DFT) is used to search the global minimum structures. A typical GA run would involve 20 populations run over 100 generations (total  $\sim$ 2000 evaluations per system). Owing to the computational cost of DFT, these studies involve system sizes of single to few unit cells. In order to use GA to predict extended defect structures such as the line defects (that extended to several nanometers), one requires a system size that is much larger (supercell  $\sim$ 20  $\times$  18–360 unit cells). This is computationally intractable with DFT. Empirical force-fields with much lower cost allow us to efficiently sample the defect configurations. Hence, we use GA and MD to understand defect dynamics of extended structures.

Similarly, there have been previous efforts on advancing microscopy techniques to characterize defect dynamics. For example, in a seminal work, Hashimoto *et al.*<sup>60</sup> show *in situ* defect formation in single graphene layers by high-resolution TEM. Meyer *et al.*<sup>61</sup> represent a major advance in using TEM to image the dynamics of light atoms and molecules on graphene. Likewise, Sim *et al.*<sup>27</sup> employs electron microscopy studies to investigate how defect structures in multilayered 2D materials differ from their monolayers. While such electron microscopy studies can capture temporal evolution, their resolution is still limited to frame speeds  $\sim$ 10 Hz and consequently cannot capture short-lived events (nanosecond time scales). Such ultrafast dynamical events are crucial for defect-driven phase transitions between semiconducting and metallic phases in TMDCs (*e.g.*, MoS<sub>2</sub>). Overall, it is not possible for a single technique to probe the dynamics occurring over disparate time and length scales.

Here, ML methods are combined with molecular dynamics simulations and model validation is performed *via* HRTEM experiments to obtain a holistic picture of how point defects organize into extended structures, which subsequently drive the 2H-to-1T transition. This understanding cannot be provided by a single method alone since the time scales involved in defect dynamics vary from picoseconds (too fast for HRTEM) to several minutes (too long for MD). By using HRTEM, GA, and MD simulations, we show the defect evolution from randomly distributed point defects to extended line defects and highlight their role in driving the 2H to 1T phase transitions in 2D MoS<sub>2</sub>. Specifically, we employ GA to identify extended defect structures that form *via* organization of point defects; the GA-identified structures are validated by HRTEM. Molecular dynamics simulations, alongside HRTEM, elucidate (a) that extended defect structures act as precursors for 2H-to-1T transition and (b) the coexistence of 2H and 1T phases in a single monolayer. In all machine learning studies, model validation is an important aspect and HRTEM serves this important purpose of validating the predictions of GA. In the subsequent sections, we provide the details of the three techniques.

**Evolutionary Structural Search.** Evolutionary searches identify the global energy minimum structure of a material along with structures that are energetically close (but higher) than the most stable structure; often, such structures are kinetically trapped depending on processing and operating condition of the material. Therefore, this method is widely used in materials design problems.<sup>36,62,63</sup> Here, we adopt an evolutionary search, *viz.*, genetic

algorithms (GA) to identify energetically favorable arrangements of vacancies in one of the S planes of a MoS<sub>2</sub> layer. In GA, candidate materials structures are mapped to a genome upon which the evolutionary operations are employed. In a single layer MoS<sub>2</sub>, a plane of Mo atoms is sandwiched between two planes of S atoms; in each S plane, the atoms are organized in a 2D triangular lattice. As the interlayer vacancy migration is associated with a very high energy barrier (>5 eV), we restrict our search space to the top layer of S atoms. To describe the vacancy distribution in a given candidate structure, we define a 2D binary genome. This genome is a string containing the current state for each site in the 2D triangular lattice; each site can be in one of the two states, namely: (a) “0” representing the absence of a S atom (vacancy) and (b) “1” indicating that site is occupied by a S atom. For a prescribed vacancy density, the evolutionary search begins with a random population of 32 candidates, each with an arbitrarily chosen but distinct genome, (*i.e.*, S-vacancy distributions). The fitness of each candidate is calculated as the potential energy of the MoS<sub>2</sub> monolayer containing a distribution of S-vacancies as defined by its 2D genome. We note that the candidate structures with lower potential energy possess higher fitness, and have higher chance of survival in an evolution. The atomic interactions in the defective MoS<sub>2</sub> structures are modeled using the reactive force field (ReaxFF)<sup>20</sup> within LAMMPS<sup>64</sup> package. In each generation, genetic operations, namely, selection, mutation, and crossover, are performed on the current population to generate 32 new candidates; details of these operations are provided elsewhere.<sup>36,47</sup> The candidates are then ranked by their fitness, and the best (fittest) 32 candidates are passed to the next generation. This procedure is iterated until the GA run converges; *i.e.*, the potential energy of the fittest candidate does not change over a long period of time (~100 generations). We note that several case studies are conducted with varying number of population size, and 32 is found to be sufficiently large to ensure necessary structural diversity in the population (in the initial stages) as well as convergence to low-energy configurations with reasonable computational costs. Our evolutionary searches using population sizes (>32) have resulted in identical lowest energy configurations, as that from runs with 32 candidates in the gene pool. Moreover, the 2D MoS<sub>2</sub> sheet used for sampling defect configurations is sufficiently large (5.2 nm × 5.8 nm) to avoid finite size effects; using a MoS<sub>2</sub> sheet with twice the area yielded identical configurations after convergence of GA runs.

**Molecular Dynamics Simulations.** To investigate the atomic-scale mechanisms underlying early stages of 2H-to-1T phase transition in monolayer MoS<sub>2</sub>, we employed isobaric-isothermal (NPT) MD at various temperatures (300–1500 K) and ambient pressure. All MD simulations are performed using the LAMMPS<sup>64</sup> package. Defective monolayer MoS<sub>2</sub> sheets (up to 21.8 nm × 24.9 nm; 17140 atoms) are prepared by placing the GA-derived energetically favorable extended vacancy configurations (mostly lines) along random orientations in one S-plane. Periodic boundary conditions are employed in the plane of the MoS<sub>2</sub> sheet. Similar to the GA searches, the atomic interactions are described by ReaxFF.<sup>20</sup> Constant temperature and pressure conditions are maintained using a Nose–Hoover thermostat and barostat.<sup>65</sup>

**Sample Preparation and High-Resolution Transmission Electron Microscopy.** Single-layer MoS<sub>2</sub> samples were prepared through an electrochemical thinning process, known as electro-ablation (EA), using the procedure reported by Das *et al.*<sup>66</sup> In the EA process, multilayer/bulk MoS<sub>2</sub> flakes are mechanically exfoliated onto a conductive TiN substrate where a 1.4 V *vs* Ag/AgCl potential was applied for <60 s. During the substrate-assisted, self-limited EA, the multilayer flakes undergo an electro-oxidation process which ablates away the bulk layers leaving the bottom monolayer intact. TMDs produced *via* EA have shown excellent semiconducting properties in field effect transistor (FET) devices; however, photoluminescence studies have shown that excessive EA times introduce significant numbers of defects such as sulfur vacancies. Since the ablation initiates at the edge sites and therefore material ablates first from the perimeter working inward toward the center of the flake, the outer edges are exposed to the EA process for longer periods of time.<sup>67–69</sup>

Hence, an inhomogenous defect density is observed as seen in Figure 2 with the edge regions being more defective than the center. The electroablated exfoliated MoS<sub>2</sub> flakes were transferred by an etchant free transfer method<sup>70</sup> from the TiN substrate onto a Au Quantifoil TEM grid for TEM analyses; in this technique, most residues are washed away by several water baths to avoid contamination. Aberration corrected scanning/TEM (AC-S/TEM) imaging was performed on a FEI Titan<sup>3</sup> 60–300 microscope at 80 kV accelerating voltage with a monochromated gun and spherical aberration corrected lenses, providing subangstrom resolution. The electron dose of ~5000 e<sup>-</sup>/Å<sup>2</sup>·s was used for HRTEM imaging of monolayer MoS<sub>2</sub> to minimize structural damage and to push away possible contaminants. The high-angle annular dark field (HAADF) detector (Fischione) which was used for ADF-STEM imaging acquisition had a beam current of 45 pA, beam convergence angle of 30 mrad, and collection angle of 51–300 mrad. The HRTEM and ADF-STEM images in the content are further filtered by Gaussian blur function *via* ImageJ software.

## ASSOCIATED CONTENT

### S Supporting Information

The Supporting Information is available free of charge on the ACS Publications website at DOI: [10.1021/acsnano.8b02844](https://doi.org/10.1021/acsnano.8b02844).

Details of the MD simulations performed for 2D MoS<sub>2</sub> (pristine as well as with sulfur defects) ([PDF](#))

## AUTHOR INFORMATION

### Corresponding Authors

\*E-mail: [sud70@psu.edu](mailto:sud70@psu.edu).

\*E-mail: [badri.narayanan@louisville.edu](mailto:badri.narayanan@louisville.edu).

\*E-mail: [skrssank@anl.gov](mailto:skrssank@anl.gov).

### ORCID

Daniel S. Schulman: [0000-0002-0751-0578](https://orcid.org/0000-0002-0751-0578)

Henry Chan: [0000-0002-8198-7737](https://orcid.org/0000-0002-8198-7737)

Mathew J. Cherukara: [0000-0002-1475-6998](https://orcid.org/0000-0002-1475-6998)

Saptarshi Das: [0000-0002-0188-945X](https://orcid.org/0000-0002-0188-945X)

Badri Narayanan: [0000-0001-8147-1047](https://orcid.org/0000-0001-8147-1047)

Subramanian K. R. S. Sankaranarayanan: [0000-0002-9708-396X](https://orcid.org/0000-0002-9708-396X)

### Present Address

<sup>¶</sup>B.N.: Department of Mechanical Engineering, University of Louisville, Louisville KY 40292

### Author Contributions

S.D., B.N., and S.K.R.S. conceived this project. T.P. carried out the GA optimization and MD simulations. F.Z. and D.S. carried out the experiments. All the authors contributed to the data analysis. S.K.R.S., B.N., and T.P. wrote this manuscript with contribution from all the authors. All authors have given approval to the final version of the manuscript.

### Notes

The authors declare no competing financial interest.

## ACKNOWLEDGMENTS

This work was supported by Argonne LDRD-2017-012-N0. Use of the Center for Nanoscale Materials and the resources of the Argonne Leadership Computing Facility was also supported by the U.S. Department of Energy (DOE), Office of Science, Office of Basic Science, under Contract No. DE-AC02-06CH11357. This research used resources of the National Energy Research Scientific Computing Center, a DOE office of science user facility supported by the Office of Science of the US Department of Energy under Contract No. DE-AC02-05CH11231. An award of computer time was

provided by the Innovative and Novel Computational Impact on Theory and Experiment (INCITE) program. This research used resources of the Argonne Leadership Computational Facility, which is a DOE Office of Science user facility supported under Contract No. DE-AC02-06CH11357. T.K.P. thanks Prof. David Simmons, University of Akron, for providing the GA code, which is modified and used for this work. D.S.S. and S.D. acknowledge support from the Air Force Office of Scientific Research (AFOSR) through the Young Investigator Program with Grant No. FA9550-17-1-0018. F. Z. and M. T. acknowledge the NSF-IUCRC Center for Atomically Thin Multifunctional Coatings 275 (ATOMIC), under award #1540018.

## REFERENCES

- (1) Bhimanapati, G. R.; Lin, Z.; Meunier, V.; Jung, Y.; Cha, J.; Das, S.; Xiao, D.; Son, Y.; Strano, M. S.; Cooper, V. R.; Liang, L.; Louie, S. G.; Ringe, E.; Zhou, W.; Kim, S. S.; Naik, R. R.; Sumpter, B. G.; Terrones, H.; Xia, F.; Wang, Y.; et al. Recent Advances in Two-Dimensional Materials beyond Graphene. *ACS Nano* **2015**, *9*, 11509–11539.
- (2) Das, S.; Robinson, J. A.; Dubey, M.; Terrones, H.; Terrones, M. Beyond Graphene: Progress in Novel Two-Dimensional Materials and van Der Waals Solids. *Annu. Rev. Mater. Res.* **2015**, *45*, 1–27.
- (3) Voiry, D.; Mohite, A.; Chhowalla, M. Phase Engineering of Transition Metal Dichalcogenides. *Chem. Soc. Rev.* **2015**, *44*, 2702–2712.
- (4) Cançado, L. G.; da Silva, M. G.; Ferreira, E. H. M.; Hof, F.; Kampiotti, K.; Huang, K.; Pénicaud, A.; Achete, C. A.; Capaz, R. B.; Jorio, A. Disentangling Contributions of Point and Line Defects in the Raman Spectra of Graphene-Related Materials. *2D Mater.* **2017**, *4*, 025039.
- (5) Zhou, W.; Zou, X.; Najmaei, S.; Liu, Z.; Shi, Y.; Kong, J.; Lou, J.; Ajayan, P. M.; Yakobson, B. I.; Idrobo, J.-C. Intrinsic Structural Defects in Monolayer Molybdenum Disulfide. *Nano Lett.* **2013**, *13*, 2615–2622.
- (6) Addou, R.; Colombo, L.; Wallace, R. M. Surface Defects on Natural MoS<sub>2</sub>. *ACS Appl. Mater. Interfaces* **2015**, *7*, 11921–11929.
- (7) Schulman, D. S.; Arnold, A. J.; Das, S. Contact Engineering for 2D Materials and Devices. *Chem. Soc. Rev.* **2018**, *47*, 3037.
- (8) McDonnell, S.; Addou, R.; Buie, C.; Wallace, R. M.; Hinkle, C. L. Defect-Dominated Doping and Contact Resistance in MoS<sub>2</sub>. *ACS Nano* **2014**, *8*, 2880–2888.
- (9) Bampoulis, P.; van Bremen, R.; Yao, Q.; Poelsema, B.; Zandvliet, H. J. W.; Sotthewes, K. Defect Dominated Charge Transport and Fermi Level Pinning in MoS<sub>2</sub>/Metal Contacts. *ACS Appl. Mater. Interfaces* **2017**, *9*, 19278–19286.
- (10) Das, S.; Chen, H.-Y.; Penumatcha, A. V.; Appenzeller, J. High Performance Multilayer MoS<sub>2</sub> Transistors with Scandium Contacts. *Nano Lett.* **2013**, *13*, 100–105.
- (11) Yu, Z.; Pan, Y.; Shen, Y.; Wang, Z.; Ong, Z.-Y.; Xu, T.; Xin, R.; Pan, L.; Wang, B.; Sun, L.; Wang, J.; Zhang, G.; Zhang, Y. W.; Shi, Y.; Wang, X. Towards Intrinsic Charge Transport in Monolayer Molybdenum Disulfide by Defect and Interface Engineering. *Nat. Commun.* **2014**, *5*, 5290.
- (12) Qiu, H.; Xu, T.; Wang, Z.; Ren, W.; Nan, H.; Ni, Z.; Chen, Q.; Yuan, S.; Miao, F.; Song, F.; Long, G.; Shi, Y.; Sun, L.; Wang, J.; Wang, X. Hopping Transport through Defect-Induced Localized States in Molybdenum Disulphide. *Nat. Commun.* **2013**, *4*, 2642.
- (13) Zhu, W.; Low, T.; Lee, Y.-H.; Wang, H.; Farmer, D. B.; Kong, J.; Xia, F.; Avouris, P. Electronic Transport and Device Prospects of Monolayer Molybdenum Disulphide Grown by Chemical Vapour Deposition. *Nat. Commun.* **2014**, *5*, 3087.
- (14) Arnold, A. J.; Razavieh, A.; Nasr, J. R.; Schulman, D. S.; Eichfeld, C. M.; Das, S. Mimicking Neurotransmitter Release in Chemical Synapses via Hysteresis Engineering in MoS<sub>2</sub> Transistors. *ACS Nano* **2017**, *11*, 3110–3118.
- (15) Sangwan, V. K.; Lee, H.-S.; Bergeron, H.; Balla, I.; Beck, M. E.; Chen, K.-S.; Hersam, M. C. Multi-Terminal Memtransistors from Polycrystalline Monolayer Molybdenum Disulfide. *Nature* **2018**, *554*, 500–504.
- (16) Lin, Y.-C.; Dumcenco, D. O.; Huang, Y.-S.; Suenaga, K. Atomic Mechanism of the Semiconducting-to-Metallic Phase Transition in Single-Layered MoS<sub>2</sub>. *Nat. Nanotechnol.* **2014**, *9*, 391.
- (17) Friedman, A. L.; Hanbicki, A. T.; Perkins, F. K.; Jernigan, G. G.; Culbertson, J. C.; Campbell, P. M. Evidence for Chemical Vapor Induced 2H to 1T Phase Transition in MoX<sub>2</sub> (X = Se, S) Transition Metal Dichalcogenide Films. *Sci. Rep.* **2017**, *7*, 3836.
- (18) Han, S. W.; Park, Y.; Hwang, Y. H.; Jekal, S.; Kang, M.; Lee, W. G.; Yang, W.; Lee, G.-D.; Hong, S. C. Electron Beam-Formed Ferromagnetic Defects on MoS<sub>2</sub> Surface along 1 T Phase Transition. *Sci. Rep.* **2016**, *6*, 38730.
- (19) Enyashin, A. N.; Yadgarov, L.; Houben, L.; Popov, I.; Weidenbach, M.; Tenne, R.; Bar-Sadan, M.; Seifert, G. New Route for Stabilization of 1T-WS<sub>2</sub> and MoS<sub>2</sub> Phases. *J. Phys. Chem. C* **2011**, *115*, 24586–24591.
- (20) Ostadhosseini, A.; Rahnamoun, A.; Wang, Y.; Zhao, P.; Zhang, S.; Crespi, V. H.; van Duin, A. C. T. ReaxFF Reactive Force-Field Study of Molybdenum Disulfide (MoS<sub>2</sub>). *J. Phys. Chem. Lett.* **2017**, *8*, 631–640.
- (21) Yan, S.; Qiao, W.; He, X.; Guo, X.; Xi, L.; Zhong, W.; Du, Y. Enhancement of Magnetism by Structural Phase Transition in MoS<sub>2</sub>. *Appl. Phys. Lett.* **2015**, *106*, 012408.
- (22) Kappera, R.; Voiry, D.; Yalcin, S. E.; Branch, B.; Gupta, G.; Mohite, A. D.; Chhowalla, M. Phase-Engineered Low-Resistance Contacts for Ultrathin MoS<sub>2</sub> Transistors. *Nat. Mater.* **2014**, *13*, 1128–1134.
- (23) Pi, Y.; Li, Z.; Xu, D.; Liu, J.; Li, Y.; Zhang, F.; Zhang, G.; Peng, W.; Fan, X. 1T-Phase MoS<sub>2</sub> Nanosheets on TiO<sub>2</sub> Nanorod Arrays: 3D Photoanode with Extraordinary Catalytic Performance. *ACS Sustainable Chem. Eng.* **2017**, *5*, 5175–5182.
- (24) Jiang, L.; Zhang, S.; Kulinich, S. A.; Song, X.; Zhu, J.; Wang, X.; Zeng, H. Optimizing Hybridization of 1T and 2H Phases in MoS<sub>2</sub>Monolayers to Improve Capacitances of Supercapacitors. *Mater. Res. Lett.* **2015**, *3*, 177–183.
- (25) Voiry, D.; Yamaguchi, H.; Li, J.; Silva, R.; Alves, D. C. B.; Fujita, T.; Chen, M.; Asefa, T.; Shenoy, V. B.; Eda, G.; Chhowalla, M. Enhanced Catalytic Activity in Strained Chemically Exfoliated WS<sub>2</sub> Nanosheets for Hydrogen Evolution. *Nat. Mater.* **2013**, *12*, 850–855.
- (26) Fan, X.; Xu, P.; Zhou, D.; Sun, Y.; Li, Y. C.; Nguyen, M. A. T.; Terrones, M.; Mallouk, T. E. Fast and Efficient Preparation of Exfoliated 2H MoS<sub>2</sub> Nanosheets by Sonication-Assisted Lithium Intercalation and Infrared Laser-Induced 1T to 2H Phase Reversion. *Nano Lett.* **2015**, *15*, 5956–5960.
- (27) Sim, D. M.; Han, H. J.; Yim, S.; Choi, M.-J.; Jeon, J.; Jung, Y. S. Long-Term Stable 2H-MoS<sub>2</sub> Dispersion: Critical Role of Solvent for Simultaneous Phase Restoration and Surface Functionalization of Liquid-Exfoliated MoS<sub>2</sub>. *ACS Omega* **2017**, *2*, 4678–4687.
- (28) Fair, K. M.; Ford, M. J. Phase Transitions and Optical Properties of the Semiconducting and Metallic Phases of Single-Layer MoS<sub>2</sub>. *Nanotechnology* **2015**, *26*, 435705.
- (29) Sun, X.; Wang, Z.; Li, Z.; Fu, Y. Q. Origin of Structural Transformation in Mono- and Bi-Layered Molybdenum Disulfide. *Sci. Rep.* **2016**, *6*, srep26666.
- (30) Cherukara, M. J.; Schulmann, D. S.; Sasikumar, K.; Arnold, A. J.; Chan, H.; Sadasivam, S.; Cha, W.; Maser, J.; Das, S.; Sankaranarayanan, S. K. R. S.; Harder, R. J. Three-Dimensional Integrated X-Ray Diffraction Imaging of a Native Strain in Multi-Layered WSe<sub>2</sub>. *Nano Lett.* **2018**, *18*, 1993–2000.
- (31) Komsa, H.-P.; Krasheninnikov, A. V. From Point to Line Defects in Two-Dimensional Transition Metal Dichalcogenides: Insights from Transmission Electron Microscopy and First-Principles Calculations. In *GraphITA: Carbon Nanostructures*; Springer: Cham, 2017; pp 71–85.

- (32) Jin, C.; Lin, F.; Suenaga, K.; Iijima, S. Fabrication of a Freestanding Boron Nitride Single Layer and Its Defect Assignments. *Phys. Rev. Lett.* **2009**, *102*, 195505.
- (33) Meyer, J. C.; Chuvilin, A.; Algara-Siller, G.; Biskupek, J.; Kaiser, U. Selective Sputtering and Atomic Resolution Imaging of Atomically Thin Boron Nitride Membranes. *Nano Lett.* **2009**, *9*, 2683–2689.
- (34) Kurasch, S.; Kotakoski, J.; Lehtinen, O.; Skákalová, V.; Smet, J.; Krill, C. E.; Krasheninnikov, A. V.; Kaiser, U. Atom-by-Atom Observation of Grain Boundary Migration in Graphene. *Nano Lett.* **2012**, *12*, 3168–3173.
- (35) Kotakoski, J.; Krasheninnikov, A. V.; Kaiser, U.; Meyer, J. C. From Point Defects in Graphene to Two-Dimensional Amorphous Carbon. *Phys. Rev. Lett.* **2011**, *106*, 105505.
- (36) Patra, T. K.; Meenakshisundaram, V.; Hung, J.-H.; Simmons, D. S. Neural-Network-Biased Genetic Algorithms for Materials Design: Evolutionary Algorithms That Learn. *ACS Comb. Sci.* **2017**, *19*, 96–107.
- (37) Algara-Siller, G.; Kurasch, S.; Sedighi, M.; Lehtinen, O.; Kaiser, U. The Pristine Atomic Structure of MoS<sub>2</sub>Monolayer Protected from Electron Radiation Damage by Graphene. *Appl. Phys. Lett.* **2013**, *103*, 203107.
- (38) Cheng, P.; Sun, K.; Hu, Y. H. Mechanically-Induced Reverse Phase Transformation of MoS<sub>2</sub> from Stable 2H to Metastable 1T and Its Memristive Behavior. *RSC Adv.* **2016**, *6*, 65691–65697.
- (39) Eda, G.; Yamaguchi, H.; Voiry, D.; Fujita, T.; Chen, M.; Chhowalla, M. Photoluminescence from Chemically Exfoliated MoS<sub>2</sub>. *Nano Lett.* **2011**, *11*, 5111–5116.
- (40) Hong, J.; Pan, Y.; Hu, Z.; Lv, D.; Jin, C.; Ji, W.; Yuan, J.; Zhang, Z. Direct Imaging of Kinetic Pathways of Atomic Diffusion in Monolayer Molybdenum Disulfide. *Nano Lett.* **2017**, *17*, 3383–3390.
- (41) Komsa, H.-P.; Kurasch, S.; Lehtinen, O.; Kaiser, U.; Krasheninnikov, A. V. From Point to Extended Defects in Two-Dimensional MoS<sub>2</sub>: Evolution of Atomic Structure under Electron Irradiation. *Phys. Rev. B: Condens. Matter Mater. Phys.* **2013**, *88*, 035301.
- (42) Saha, D.; Mahapatra, S. Atomistic Modeling of the Metallic-to-Semiconducting Phase Boundaries in Monolayer MoS<sub>2</sub>. *Appl. Phys. Lett.* **2016**, *108*, 253106.
- (43) Masubuchi, S.; Morimoto, M.; Morikawa, S.; Onodera, M.; Asakawa, Y.; Watanabe, K.; Taniguchi, T.; Machida, T. Autonomous Robotic Searching and Assembly of Two-Dimensional Crystals to Build van Der Waals Superlattices. *Nat. Commun.* **2018**, *9*, 1413.
- (44) Lin, X.; Si, Z.; Fu, W.; Yang, J.; Guo, S.; Cao, Y.; Zhang, J.; Wang, X.; Liu, P.; Jiang, K.; Zhang, Y.; Zhao, W. Intelligent Identification of Two-Dimensional Structure by Machine-Learning Optical Microscopy. *ArXiv180302062 Cond-Mat* **2018**.
- (45) Wang, C. C.; Pilania, G.; Boggs, S. A.; Kumar, S.; Breneman, C.; Ramprasad, R. Computational Strategies for Polymer Dielectrics Design. *Polymer* **2014**, *55*, 979–988.
- (46) Zhu, Q.; Sharma, V.; Oganov, A. R.; Ramprasad, R. Predicting Polymeric Crystal Structures by Evolutionary Algorithms. *J. Chem. Phys.* **2014**, *141*, 154102.
- (47) Meenakshisundaram, V.; Hung, J.-H.; Patra, T. K.; Simmons, D. S. Designing Sequence-Specific Copolymer Compatibilizers Using a Molecular-Dynamics-Simulation-Based Genetic Algorithm. *Macromolecules* **2017**, *50*, 1155–1166.
- (48) Botu, V.; Batra, R.; Chapman, J.; Ramprasad, R. Machine Learning Force Fields: Construction, Validation, and Outlook. *J. Phys. Chem. C* **2017**, *121*, 511–522.
- (49) Cherukara, M. J.; Narayanan, B.; Kinaci, A.; Sasikumar, K.; Gray, S. K.; Chan, M. K. Y.; Sankaranarayanan, S. K. R. S. *Ab Initio*-Based Bond Order Potential to Investigate Low Thermal Conductivity of Stanene Nanostructures. *J. Phys. Chem. Lett.* **2016**, *7*, 3752–3759.
- (50) Narayanan, B.; Chan, H.; Kinaci, A.; Sen, F. G.; Gray, S. K.; Chan, M. K. Y.; Sankaranarayanan, S. K. R. S. Machine Learnt Bond Order Potential to Model Metal–Organic (Co–C) Heterostructures. *Nanoscale* **2017**, *9*, 18229–18239.
- (51) Zhang, Z.; Schwanz, D.; Narayanan, B.; Kotiuga, M.; Dura, J. A.; Cherukara, M.; Zhou, H.; Freeland, J. W.; Li, J.; Sutarto, R.; He, F.; Wu, C.; Zhu, J.; Sun, Y.; Ramadoss, K.; Nonnenmann, S. S.; Yu, N.; Comin, R.; Rabe, K. M.; Sankaranarayanan, S. K. R. S.; et al. Perovskite Nickelates as Electric-Field Sensors in Salt Water. *Nature* **2018**, *553*, 68–72.
- (52) Erdemir, A.; Ramirez, G.; Eryilmaz, O. L.; Narayanan, B.; Liao, Y.; Kamath, G.; Sankaranarayanan, S. K. R. S. Carbon-Based Tribofilms from Lubricating Oils. *Nature* **2016**, *536*, 67–71.
- (53) Asadi, M.; Sayahpour, B.; Abbasi, P.; Ngo, A. T.; Karis, K.; Jokisaari, J. R.; Liu, C.; Narayanan, B.; Gerard, M.; Yasaei, P.; Hu, X.; Mukherjee, A.; Lau, K. C.; Assary, R. S.; Khalili-Araghi, F.; Klie, R. F.; Curtiss, L. A.; Salehi-Khojin, A. A Lithium–Oxygen Battery with a Long Cycle Life in an Air-like Atmosphere. *Nature* **2018**, *555*, 502–506.
- (54) Bahns, J. T.; Sankaranarayanan, S. K. R. S.; Gray, S. K.; Chen, L. Optically Directed Assembly of Continuous Mesoscale Filaments. *Phys. Rev. Lett.* **2011**, *106*, 095501.
- (55) Bahns, J. T.; Sankaranarayanan, S. K. R. S.; Giebink, N. C.; Xiong, H.; Gray, S. K. Optically Directed Mesoscale Assembly and Patterning of Electrically Conductive Organic–Inorganic Hybrid Structures. *Adv. Mater.* **2012**, *24*, OP242–OP246.
- (56) Deringer, V. L.; Bernstein, N.; Bartók, A. P.; Cliffe, M. J.; Kerber, R. N.; Marbella, L. E.; Grey, C. P.; Elliott, S. R.; Csányi, G. Realistic Atomistic Structure of Amorphous Silicon from Machine-Learning-Driven Molecular Dynamics. *J. Phys. Chem. Lett.* **2018**, *9*, 2879.
- (57) Xiang, H. J.; Wei, S.-H.; Gong, X. G. Structural Motifs in Oxidized Graphene: A Genetic Algorithm Study Based on Density Functional Theory. *Phys. Rev. B: Condens. Matter Mater. Phys.* **2010**, *82*, 035416.
- (58) Gu, T.; Luo, W.; Xiang, H. Prediction of Two-Dimensional Materials by the Global Optimization Approach: Prediction of Two-Dimensional Materials by the Global Optimization Approach. *WIREs Comput. Mol. Sci.* **2017**, *7*, No. e1295.
- (59) Sanz-Navarro, C. F.; Åstrand, P.-O.; Chen, D.; Rønning, M.; van Duin, A. C. T.; Goddard, W. A. Molecular Dynamics Simulations of Metal Clusters Supported on Fishbone Carbon Nanofibers. *J. Phys. Chem. C* **2010**, *114*, 3522–3530.
- (60) Hashimoto, A.; Suenaga, K.; Gloter, A.; Urata, K.; Iijima, S. Direct Evidence for Atomic Defects in Graphene Layers. *Nature* **2004**, *430*, 870–873.
- (61) Meyer, J. C.; Girit, C. O.; Crommie, M. F.; Zettl, A. Imaging and Dynamics of Light Atoms and Molecules on Graphene. *Nature* **2008**, *454*, 319–322.
- (62) Kinaci, A.; Narayanan, B.; Sen, F. G.; Davis, M. J.; Gray, S. K.; Sankaranarayanan, S. K. R. S.; Chan, M. K. Y. Unraveling the Planar–Globular Transition in Gold Nanoclusters through Evolutionary Search. *Sci. Rep.* **2016**, *6*, 34974.
- (63) Chua, A. L.-S.; Benedek, N. A.; Chen, L.; Finnis, M. W.; Sutton, A. P. A Genetic Algorithm for Predicting the Structures of Interfaces in Multicomponent Systems. *Nat. Mater.* **2010**, *9*, 418–422.
- (64) Plimpton, S. Fast Parallel Algorithms for Short-Range Molecular Dynamics. *J. Comput. Phys.* **1995**, *117*, 1–19.
- (65) Martyna, G. J.; Klein, M. L.; Tuckerman, M. Nosé–Hoover Chains: The Canonical Ensemble via Continuous Dynamics. *J. Chem. Phys.* **1992**, *97*, 2635–2643.
- (66) Das, S.; Bera, M. K.; Tong, S.; Narayanan, B.; Kamath, G.; Mane, A.; Paulikas, A. P.; Antonio, M. R.; Sankaranarayanan, S. K. R. S.; Roelofs, A. K. A Self-Limiting Electro-Ablation Technique for the Top-Down Synthesis of Large-Area Monolayer Flakes of 2D Materials. *Sci. Rep.* **2016**, *6*, 28195.
- (67) Huang, Y.-T.; Dodd, A.; Schulman, D. S.; Sebastian, A.; Zhang, F.; Buzzell, D.; Terrones, M.; Feng, S.-P.; Das, S. Anomalous Corrosion of Bulk Transition Metal Diselenides Leading to Stable Monolayers. *ACS Appl. Mater. Interfaces* **2017**, *9*, 39059–39068.
- (68) Schulman, D. S.; Sebastian, A.; Buzzell, D.; Huang, Y.-T.; Arnold, A. J.; Das, S. Facile Electrochemical Synthesis of 2D

Monolayers for High-Performance Thin-Film Transistors. *ACS Appl. Mater. Interfaces* **2017**, *9*, 44617–44624.

(69) Schulman, D. S.; May-Rawding, D.; Zhang, F.; Buzzell, D.; Alem, N.; Das, S. Superior Electro-Oxidation and Corrosion Resistance of Monolayer Transition Metal Disulfides. *ACS Appl. Mater. Interfaces* **2018**, *10*, 4285–4294.

(70) Zhang, F.; Erb, C.; Runkle, L.; Zhang, X.; Alem, N. Etchant-Free Transfer of 2D Nanostructures. *Nanotechnology* **2018**, *29*, 025602.